

# The signature of high-velocity gas in the spectra of NGC 4151

M. Contini<sup>1,2</sup>, S. M. Viegas<sup>2</sup>, and M. A. Prieto<sup>3</sup>

<sup>1</sup> School of Physics & Astronomy, Tel Aviv University, 69978 Tel Aviv, Israel

<sup>2</sup> Instituto Astronômico e Geofísico, USP, Av. Miguel Stefano 4200, 04301-904 São Paulo, Brazil

<sup>3</sup> European Southern Observatory, 85748 Garching, Germany

Received 5 July 2001 / Accepted 5 February 2002

**Abstract.** The multiwavelength emission spectrum and associated velocity field of the Seyfert prototype NGC 4151 is modeled. Since the thirties NGC 4151 has been the subject of extensive modeling, nuclear photoionization being the basic approach considered by all authors. HST data has impressively revealed the existence of a large range of velocities ( $100\text{--}1500\text{ km s}^{-1}$ ) dominating the emitting clouds in the extended emission line region of the galaxy. Following this observational result, a revision of the photoionization modeling approach applied to NGC 4151 is presented. It is concluded that a mixture of radiation-dominated clouds and shock-dominated clouds are required to explain the multiwavelength line and continuum spectra of the galaxy. The relative contribution of shock excitation versus photoionization is consistently modeled along the nebulae taking into account the spatial variation of both flux and velocity of main optical and UV lines. The multiwavelength continuum spectrum of NGC 4151 is then nicely accounted for by a combination of nuclear emission at high energy, gas Bremsstrahlung, and dust emission. The last two phenomena are directly linked to the composite shock and photoionization excitation of the gas. The radio SED however is found dominated by synchrotron emission created by the Fermi mechanism at the shock front. In addition, a  $3 \times 10^3\text{ K}$  black body component accounts for the host galaxy contribution. As a result of the modeling, silicon is found depleted by a high factor and included in dust grains, while the N/C abundance ratio is found compatible with cosmic values.

**Key words.** galaxies: nuclei – galaxies: Seyfert – shock waves – galaxies: individual: NGC 4151 – X-ray: galaxies

## 1. Introduction

Detailed imaging of the narrow-line region (NLR) of Seyfert galaxies with the *Hubble Space Telescope* (HST) has revealed its complex morphology and velocity field. Recently, observations of NGC 4151 indicated the presence of emitting clouds with velocities ranging from  $+846$  to  $-1716\text{ km s}^{-1}$  (Winge et al. 1997; Kaiser et al. 1999).

NGC 4151 is a nearby barred galaxy, usually classified as a Seyfert type 1, although it has already been considered as a Seyfert 1.5 (Osterbrock & Koski 1976) and has also shown the characteristics of a Seyfert 2 galaxy (Penston & Pérez 1984). NGC 4151 is one of the most observed active galactic nuclei (AGN), from radio to X-rays. The recent HST longslit emission-line data (Nelson et al. 2000), coupled to ISO data (Alexander et al. 1999), offer an excellent opportunity to improve our understanding of the NLR physical conditions with the added effect of the velocity field.

The kinematics derived from the long slit observations (Nelson et al. 2000; Crenshaw et al. 2000) show evidence of three components: a low velocity system, consistent with normal disk rotation, a high velocity system in radial outflow at a few hundred  $\text{km s}^{-1}$  and an additional high velocity system with velocities up to  $1400\text{ km s}^{-1}$ , as previously found from STIS slitless spectroscopy (Hutchings et al. 1998, 1999; Kaiser et al. 1999). The authors see the signature of a radial outflow, with no interaction with the radio jet. However, high velocity components, shifted up to about  $1500\text{ km s}^{-1}$  from the systemic velocity, are also seen by Winge et al. (1997) associated with individual clouds located preferentially along the edges of the radio knots. Such association suggests a cloud-jet interaction, which definitively may influence the morphology and the physical conditions of the NLR.

The high spatial resolution permits us to see that the emission line ratios vary substantially on scales of a few tenths of an arcsecond, indicating that the density and ionization state of the emitting gas are strongly influenced by the local conditions, hence suggesting that shock fronts may be at work.

---

Send offprint requests to: M. Contini,  
e-mail: [contini@ccsg.tau.ac.il](mailto:contini@ccsg.tau.ac.il)

The presence of high-velocity clouds in the NLR of active galaxies has been predicted from the modeling of the emission-line and continuum spectra of the Seyfert 2 objects NGC 5252 and Circinus (Contini et al. 1998a, 1998b), as well as suggested from the more general analysis of the optical-ultraviolet continuum of a relatively large sample of Seyfert 2 galaxies (Contini & Viegas 2000). High velocity clouds are also invoked in an alternative model based on a multiwavelength analysis of the emission-line and continuum spectra of the source (Contini & Viegas 1999), which explains the soft X-ray excess in NGC 4051.

In all of these models the physical conditions of the high velocity clouds are usually shock-dominated. The shocks contribute to the high ionization emission-lines and to the continuum emission, mainly by providing efficient heating of dust, contributing to reproduce the observed middle-infrared emission, and to the observed soft X-ray spectrum which originates in the high temperature post-shock zone.

Yet, the interpretation of the NGC 4151 emission-line and continuum spectra so far rests exclusively on photoionization models. All the authors agree that, given the simplicity of the models, the observed line ratios can be reproduced.

In NGC 4151 the high velocity clouds are directly observed. Velocities of  $\sim 1500 \text{ km s}^{-1}$  could be theoretically explained extrapolating to the NLR the arguments about high velocity clouds raised by Weymann et al. (1997). Here, however, in order to obtain a large range of velocities, collisions are invoked.

Although photoionization models reproduce within better than a factor of 2 the most important line ratios (Schulz 1988, 1990; Kraemer et al. 2000; Alexander et al. 1999), some questions remain still open, as for example the mere fact of the influence of the velocity field in the cloud spectrum. Thus, in this paper we will look for the signature of the high velocity gas in the emission-line spectrum, as well as in the radio to X-ray continuum spectral energy distribution (SED).

We present a new type of single-cloud modeling based on the spatial distribution of the observational data in the optical range; then, a multi-cloud model is proposed to explain the emission lines in the IR.

As was done previously in modeling other objects (NGC 5252, Circinus), the multi-cloud model issued from the analysis of the emission lines is then constrained by fitting the continuum SED in a large frequency range. This is possible only with composite models (shock + photoionization), because the gas heated only by the radiation from the active center cannot reach temperatures high enough to fit the Bremsstrahlung emission and dust reradiation in the large range of the observed frequencies.

A review focused in the successes and problems of photoionization models is presented in Sect. 2. The composite models, coupling photoionization and shocks, are described in Sect. 3. The optical emission-line spectrum is discussed in Sect. 4, while the infrared lines are presented in Sect. 5, and the results for the ultraviolet lines appear

in Sect. 6. The observed and calculated SED are compared in Sect. 7, and the conclusions appear in Sect. 8.

## 2. A brief review of photoionization models

Most recently, photoionization models for the NLR of NGC 4151 have been proposed by Alexander et al. (1999) and Kraemer et al. (2000). In both cases, the observed emission-line ratios are reproduced within a factor of 2. Both set of authors use, however, different modeling approach: the matter distribution adopted is different. In Alexander's et al. (1999) models (hereinfter called type A), the best fit is found with a single cloud component with a filling factor less than unity; in Kraemer's et al. (2000) models (type B), a multi-cloud is used, namely a less dense matter-bound component is added to a dense radiation-bounded component. We note that Alexander et al. discarded this latter solution arguing that a matter-bounded component implies three free additional parameters, whereas the introduction of a filling factor – their case – implies only one. Nevertheless, let us recall that a matter-bounded component favors the high ionization lines, while (radiation-bounded) models with filling-factor less than unity mimic a lower average density, leading to a larger ionized zone and favoring the low-ionization lines. Thus, models assuming a filling factor less than unity are not a good physical representation of a clumpy zone; yet, the spatial distribution of [SII] ratios across NGC 4151 extended emission line region reveals instead a rather clumpy region with regions of higher and lower density at different points along the HST slit (Nelson et al. 2000). Regarding both type A and type B models, the authors agree that “the fit of the line ratios is good *taking into account the simplicity of the models*”.

Simplicity has always been a strong argument in favor of photoionization models applied to nebular regions in AGNs, in addition to the undisputable presence of a strong central radiation source. However, in Science it is usually from the attempt to explain the “imperfections” of a model, (those data not explained by it), that a more realistic scenario can be drawn. With that in mind we list below the discrepancies between the above proposed photoionization models and the observational data of NGC 4151.

Due to the various difficulties to have a self-consistent data set (data from different epoch, different resolutions and apertures), Alexander et al. (1999) use several criteria to select the set of emission-lines to be reproduced by type A models. One of the criteria excludes lines emitted by ions that “*can be easily ionized by other processes*”. The set of emission-lines excluded includes some usually used in the diagnostic diagrams of nebular gas: He II 4686, [O III] 4363, [O I] 6300, [N II] 6548+6584 and the density indicator [SII] 6716, 6731 doublet, in addition to the high-ionization Fe lines: [Fe X] 6734 and [Fe XI] 7892. The final set of lines used for modeling, that includes UV, optical, and IR lines, is reproduced within a factor of 2 by their best fit models. Discrepancies larger than two are derived for [Fe VII] 5721, [Fe VII] 6086, [Ne II] 12.8 and [Ne III]

36.0 which are underpredicted, and for [S III] 9069, [Ne V] 14.3, [S III] 18.7, [Ne V] 24.3, and [S III] 33.5 that are overpredicted.

Regarding the SED implied by models, the presence of a *big blue bump* in the ionizing radiation spectrum, peaking at 50 eV, is excluded by their best-fit model because its effect would be *to overproduce the low-ionization lines and underproduce the high-ionization lines*. However, this is the net effect produced by imposing a filling factor less than unity, as adopted in their best-fit model.

Kraemer et al. models (type B) use HST/STIS low-dispersion long-slit data at position angle  $PA = 221^\circ$ . Thus, their data set includes UV and optical lines, but no infrared lines that are the basis of type A models by Alexander et al. (1999). Their model results are compared with observed emission-line ratios derived at different positions along the slit. The large majority of the lines are reproduced within a factor of 2. Divergencies larger than 2 are often found for the high ionization lines: [Fe VII] lines, and the UV lines N V 1240, [Ne IV] 2423, and NIV] 1486, although in the latter case the signal-to-noise is very low. At some locations of the emitting nebulae, the calculated C III] 1909, C II] 2326, [O III] 4363, and the [S III] lines, also largely diverge from the data. Notice, however, that C III] and C II] are blended and that, in the case of the [S III] lines, the discrepancy may be due to an instrumental effect, as pointed out by Kraemer et al. (2000).

Several interpretations for the above discrepancies are discussed by Kraemer et al. (2000). Our assumption is that those discrepancies may be revealing the presence of an additional ionizing mechanism, which is not the dominant process, but that shows its signature through particular observational features. This point of view is adopted here assuming that the additional mechanism is due to the presence of shocks.

### 3. Single-cloud models

Faint high velocity emission regions intermingled with brighter emission clouds are shown in NGC 4151 imaging (Hutchings et al. 1999). We consider this observational fact as an indication that the extended NLR of NGC 4151 is a mixture of low velocity radiation-dominated clouds and high velocity shock-dominated clouds, all contributing to the emission-line spectrum. Accordingly, composite models accounting for the coupled effect of the central ionizing radiation and shock excitation due to cloud motions are assumed. Numerical simulations for single clouds are obtained with the SUMA code (see, for instance, Viegas & Contini 1994). Notice that the simulations apply whether the shocks originate from an interaction of the emitting clouds with the radio jet or from a radial outflow of the clouds.

The input parameters are the shock velocity,  $V_s$ , the preshock density,  $n_0$ , the preshock magnetic field,  $B_0$ , the ionizing radiation spectrum, the chemical abundances, the dust-to-gas ratio by number,  $d/g$ , and the geometrical thickness of the clouds,  $D$ . A power-law, characterized

by the power index  $\alpha$  and the flux,  $F_H$ , at the Lyman limit, reaching the cloud (in units of  $\text{cm}^{-2} \text{s}^{-1} \text{eV}^{-1}$ ) is generally adopted. For all the models,  $B_0 = 10^{-4}$  Gauss,  $\alpha_{UV} = 1.5$ , and  $\alpha_X = 0.4$ , and cosmic abundances (Allen 1973) are adopted. The basic models are calculated with  $d/g = 10^{-15}$ , however, this value is changed a posteriori to better fit the continuum SED.

Shock dominated models (SD) are calculated assuming that the effects of the shock prevail on radiation ( $F_H = 0$ ). Radiation dominated models (RD), however, are composite, i.e. they account both for photoionization and shocks up to  $V_s = 500 \text{ km s}^{-1}$ , but photoionization dominates the physical conditions of the emitting gas.

The grid of models which are actually used for modeling is presented in an accompanying paper by Contini & Viegas (2001, hereafter referred to as CV01). In the following, calculated emission-line ratios from a selected number of models in the grid are compared to the HST log-slit optical data at  $PA = 221^\circ$  (Nelson et al. 2000; Kraemer et al. 2000) and to the ISO integrated aperture SWS data by Sturm et al. (1999). Models are selected on the basis of the physical conditions of the emitting gas dictated by the observations, e.g. the FWHM of the line profiles for  $V_s$ .

In models which account for shock effects, the density downstream is determined by compression, which depends on the shock velocity, and changes considerably with distance from the shock front (CV01, Figs. 5a, 6a, and 7a). Therefore, the preshock density and the shock velocity chosen define a distribution of the density across the cloud, which must be adequate to provide a good fit to the density sensitive lines, e.g., [O II] 3727, [N I] 5200, [N II] 6548 ([S II] 6716+ is not very significant because S can be locked in dust grains).

Moreover, in the NLR, the density of the clouds follows the gradient of the cloud velocity, decreasing with the distance to the center. For each cloud, the observed [S II] 6717/6730 line ratio (which does not depend on S/H) is used as a first test for the choice of  $n_0$  and  $V_s$ . Then, the intensity of the ionizing radiation, the physical conditions calculated by the model, and the geometrical thickness of the cloud are deduced from the line spectrum, as a whole. The [O III]/ $H\beta$  line ratio is an indicator for  $F_H$ . On the other hand, wide clouds are optically thick, leading to stronger low ionization level lines, while narrow clouds are matter-bounded, with fainter low-ionization lines. Thus the choice of  $D$  is then constrained by the best fit of a large number of line ratios, particularly, the ratio of the low ionization lines to  $H\beta$ .

### 4. The optical emission-lines

#### *Modeling the spatial distribution*

Because of the availability of spatially resolved emission-line spectra in different regions of NGC 4151, a new modeling approach is followed in this work. The most significant optical emission lines are modeled accounting for their spatial distribution across the NLR.

In each position we check the consistency of the prevailing models explaining several line ratios, including those that are poorly reproduced by the photoionization models.

The observed and calculated emission-line intensities relative to  $H\beta$  are presented in a series of figures (Figs. 1–4), where the emission-line ratios are shown as a function of the projected nuclear distance, including both the SW data (on the left) and the NE data (on the right) at  $PA = 221^\circ$ .

In order to determine the intensity of the power-law radiation flux in the NLR edge closer to the nucleus a preliminary estimate is made by comparing model results with the observed line ratios as presented in Fig. 1. Filled squares refer to Nelson et al. (2000) (not reddening corrected) and filled triangles to Kraemer et al. (2000) (reddening corrected) data, respectively.

The scales for  $\log F_H$  are indicated upon the upper horizontal axis. Each curve represents RD models calculated with different  $F_H$  but corresponding to the same  $V_s$ - $n_0$ :  $V_s = 100 \text{ km s}^{-1}$  and  $n_0 = 100 \text{ cm}^{-3}$  (dotted lines),  $V_s = 200 \text{ km s}^{-1}$  and  $n_0 = 200 \text{ cm}^{-3}$  (dash-dotted lines),  $V_s = 300 \text{ km s}^{-1}$  and  $n_0 = 300 \text{ cm}^{-3}$  (short-dash lines),  $V_s = 500$  and  $n_0 = 300 \text{ cm}^{-3}$ , (long-dash lines). Thin lines refer to a narrow cloud ( $D = 10^{17-18} \text{ cm}$ ) and thick lines to wider clouds ( $D = 10^{19} \text{ cm}$ ).

A sequence of three different cases ( $\log F_H = 13, 12$ , and  $11.3$ ) is shown in the top, middle, and bottom diagrams, respectively. We have chosen the  $[OIII]/H\beta$  and  $[OII]/H\beta$  line ratios, because are the most significant. The fit of both  $[OIII]/H\beta$  and  $[OII]/H\beta$  data is acceptable only in the bottom diagrams (notice that in these diagrams the flux is not fully symmetric, indicating that the SW and NE regions are slightly different). So, for consistency we chose the bottom case to model also the other line ratios.

Since we are investigating the intensity of ionizing radiation from the active center (AC) and the velocity distribution in the central region of NGC 4151, both  $F_H$  and  $V_s$  are shown in Figs. 2–4 diagrams. In this way, the relative importance of the velocity field and the AC radiation field can be recognized. The scales for  $\log F_H$  and  $V_s$  (in  $\text{km s}^{-1}$ ) are indicated upon the horizontal upper axis of the top and middle and bottom diagrams, respectively.

In the top diagrams of Figs. 2–4 (panels a and d) each line corresponds to RD model results as in Fig. 1. Panels b and e show the solid lines corresponding to SD models (CV01, Tables 1–10) for which the maximum value of the velocity distribution is  $V_s = 700 \text{ km s}^{-1}$  in the central region, while diagrams c and f correspond to the results with a maximum velocity of  $V_s = 1400 \text{ km s}^{-1}$ .

Because shock dominated models for narrow and wide clouds give very similar results, these models are represented by one line (model results overlap), corresponding to one serie of results. We draw attention to the thin and thick lines in the two bottom diagrams which refer to reduced and full intensity line ratios, respectively, and not

to models calculated by small and large  $D$ , as shown in the top diagrams.

The model results shown in Figs. 2–4 cover most of the data consistently for the  $[O III] 5007+4959/H\beta$ ,  $[O II] 3727/H\beta$ ,  $[O I] 6300+6363/H\beta$ ,  $[S III] 9069/H\beta$ ,  $[S II] 6713+6731/H\beta$ , and  $[Fe VII] 6086/H\beta$  line ratios. The first three ratios are related to the ionization state of the gas, while the other three are chosen because they are not well reproduced by pure photoionization models.

The ranges and the spatial distributions of  $F_H$  were chosen phenomenologically by the fit, particularly, of the  $[O III]/H\beta$  and  $[S III]/H\beta$  ratios, while the ranges and the distributions of  $V_s$  were chosen by fitting the low ionization ( $[O II]/H\beta$ ,  $[S II]/H\beta$ ) and neutral ( $[O I]/H\beta$ ) line ratios. The data corresponding to the high ionization line ratio  $[Fe VII]/H\beta$  are not enough to constrain the models.

We adopt a velocity field decreasing from the center of the galaxy outwards. The observed velocity field is, however, complex, so, two different shock velocity distributions are shown, one with a maximum  $V_s \sim 700 \text{ km s}^{-1}$  in the central region (middle diagrams), and another with a higher maximum  $V_s$ , up to  $1400 \text{ km s}^{-1}$  (bottom diagrams).

Two different lines represent the SD models in both middle and bottom diagrams. The thick one corresponds to the calculated models, the thin one to the models downwards shifted by a factor of 3 (middle diagrams) and of 2 (bottom diagrams). The shift in the middle diagram is dictated by the fit of the  $[O I]/H\beta$  ratios (see Sect. 4.1) and in the bottom diagram by the  $[Fe VII]/H\beta$  ratios (see Sect. 4.3). These shifts do not represent lower abundances of the elements relative to H, but they indicate that in a multi-cloud model corresponding to the weighted sum of single-cloud models, the weights of the SD high velocity ( $>300 \text{ km s}^{-1}$ ) clouds is reduced (see Sect. 5). Indeed, by modeling the data on a large scale, this solution may look arbitrary, particularly considering faint lines (e.g.  $[O I]$ ), and lines affected by the presence of dust (e.g.  $[S III]$ ,  $[S II]$ , etc.). If reducing the weights of the SD models, the fit of all the emission-lines is consistently improved, we can conclude that this reduction is sound and SD models corresponding to high velocities in the nuclear region have lower weights. The relative weight accounts for the relative number of clouds in the conditions determined by the model, for the dilution factor (i.e., the square ratio between the distance of the cloud from the galaxy center) and the distance of the galaxy from Earth. Notice that the middle and bottom diagrams in Figs. 2–4 refer to “high velocities” in the nuclear region of the galaxy (between  $1500$ – $700 \text{ km s}^{-1}$  and about  $300 \text{ km s}^{-1}$ ). Indeed, Nelson et al. (2000, Fig. 5) show that the bulk of cloud velocities is within  $300 \text{ km s}^{-1}$ . So, the reduction of the weights in the SD diagrams indicates that the number of high velocity SD clouds is small.

Recall that observational data result from the integration along the line of sight, which may include different clouds. Thus, a more realistic fit should be obtained by a multi-cloud average (see Sect. 5). A compromise between

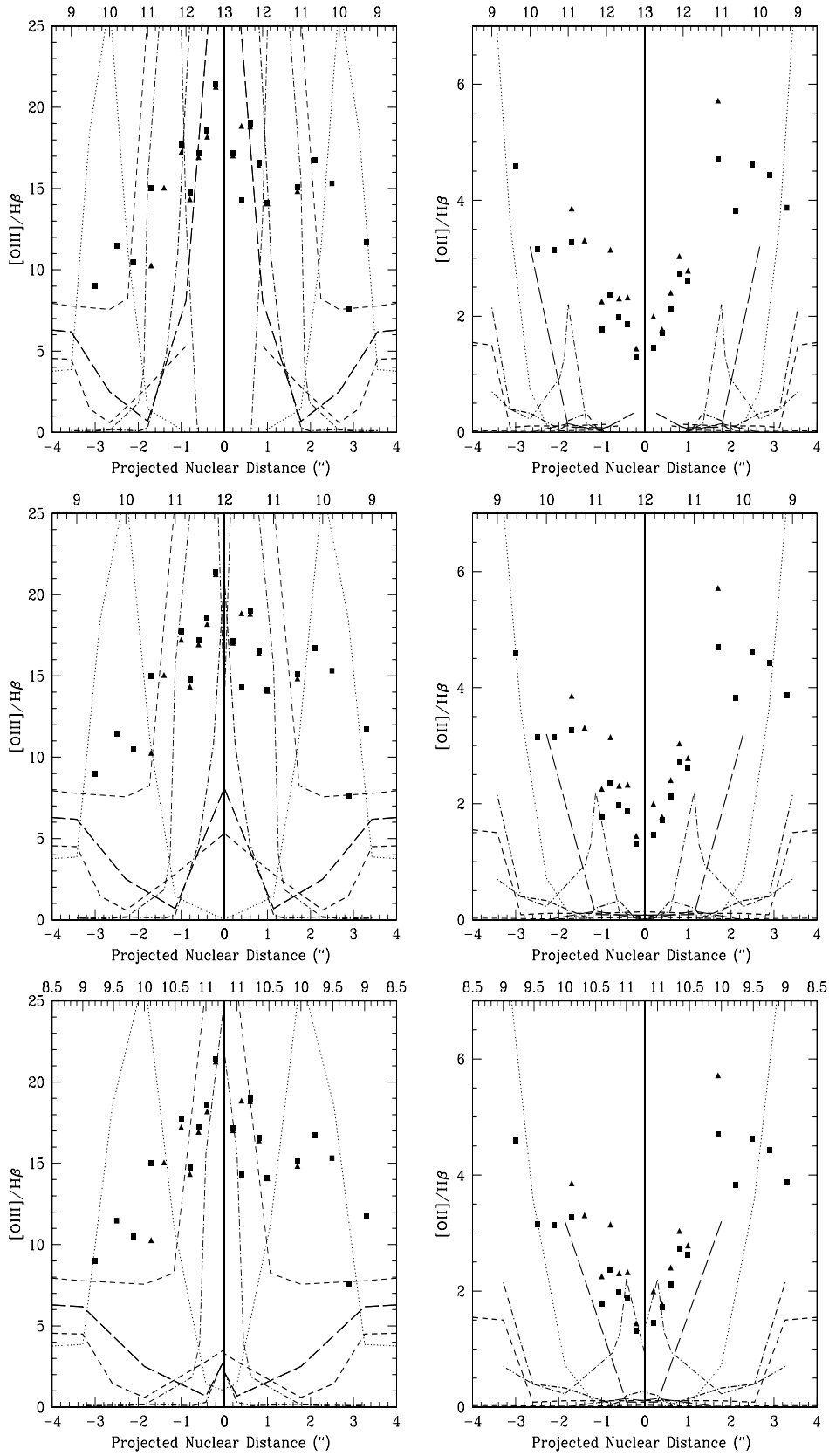


**Fig. 1.** The  $[O\ III] \ 5007+4959/H\beta$  (left diagrams) and the  $[O\ II] \ 3727/H\beta$  (right diagrams) emission-line ratios are shown as a function of the projected nuclear distance.

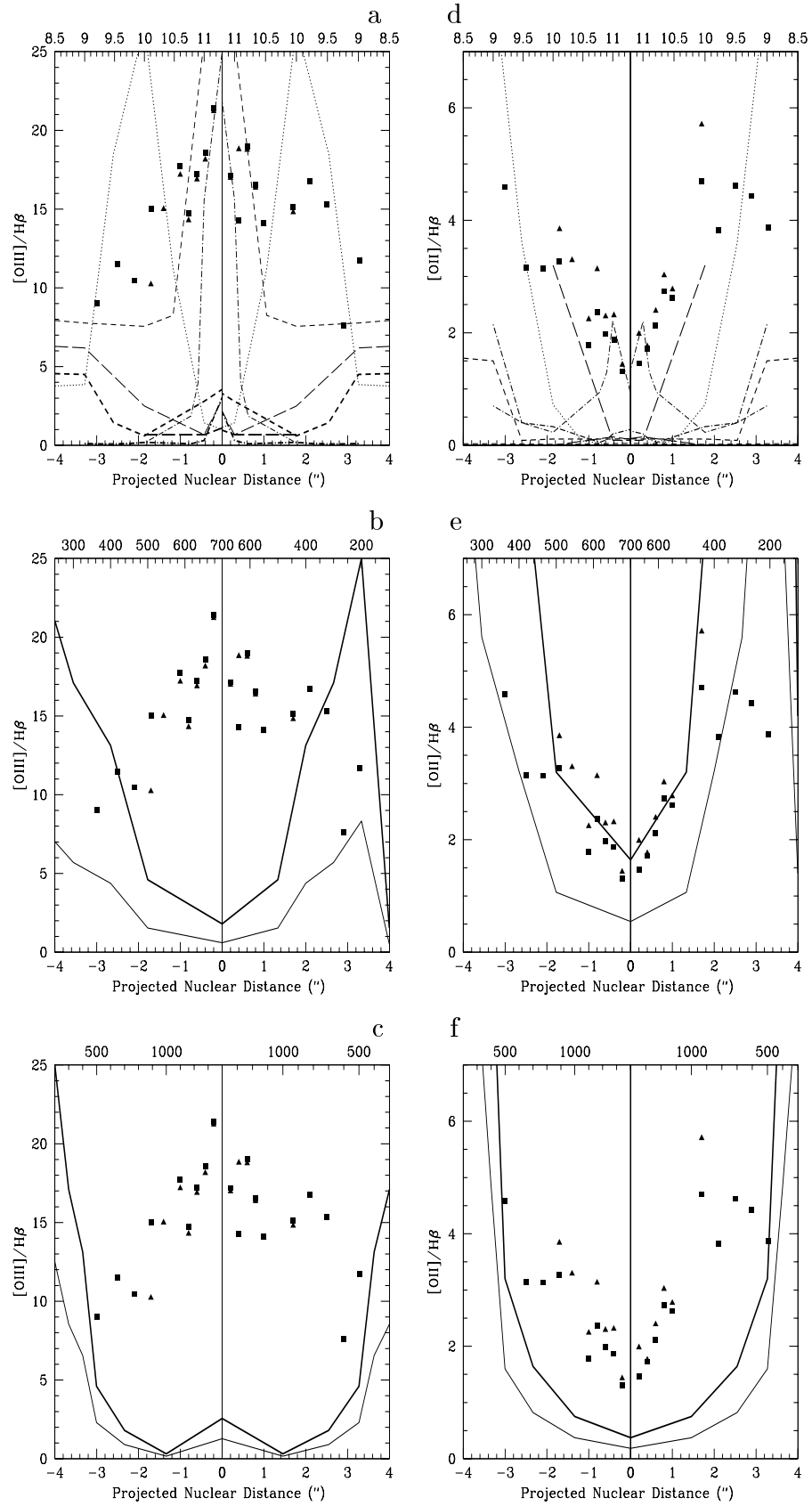


**Fig. 2.** The [O III] 5007+4959/H $\beta$  (left) and the [O II] 3727/H $\beta$  (right) emission-line ratios are shown as a function of the projected nuclear distance. Same notation as in Fig. 1.

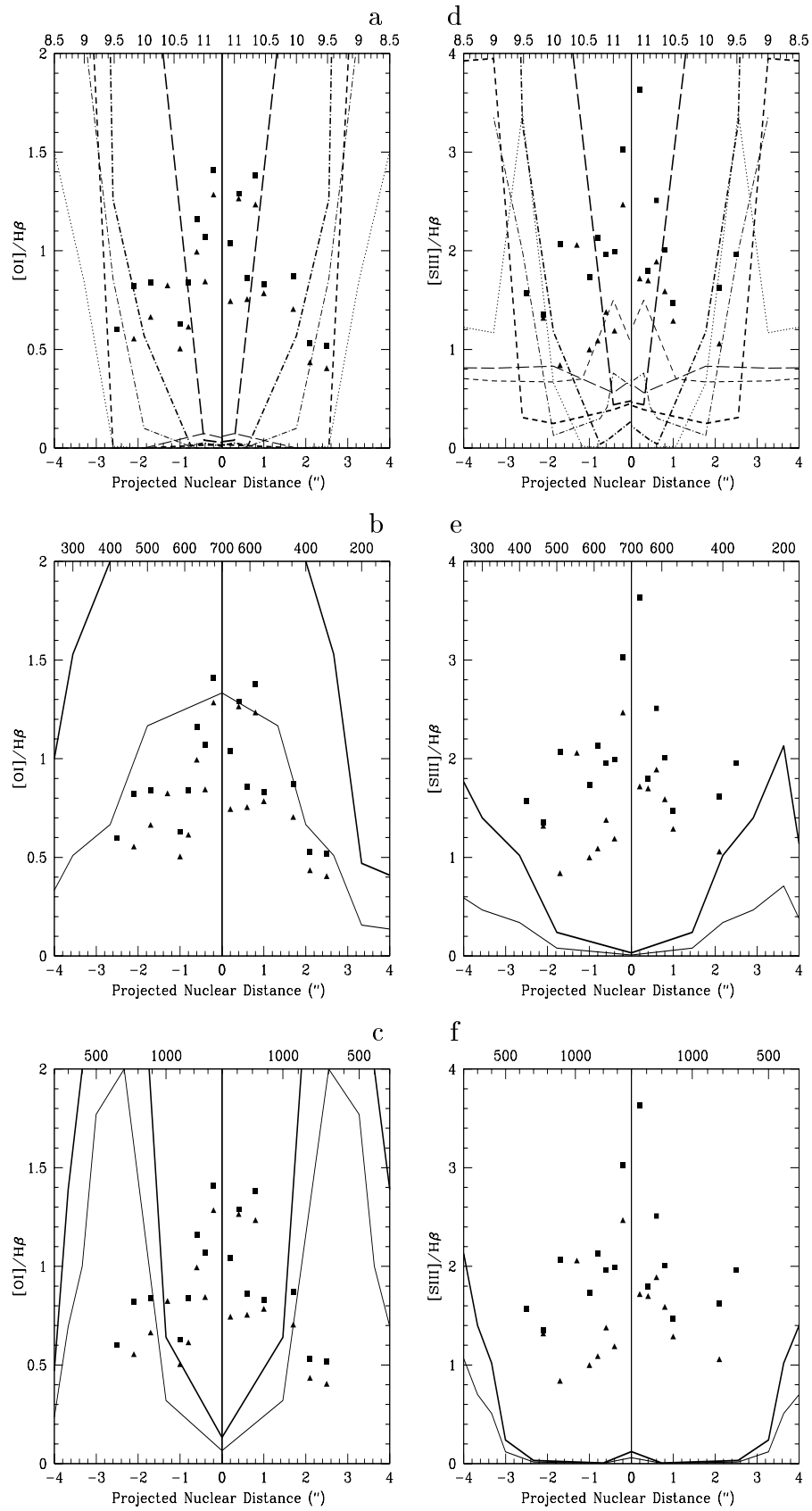


**Fig. 3.** The [O I] 6300+6360/H $\beta$  (left) and the [S III] 9069/H $\beta$  (right) emission-line ratios as a function of the projected nuclear distance. Same notation as in Fig. 1.

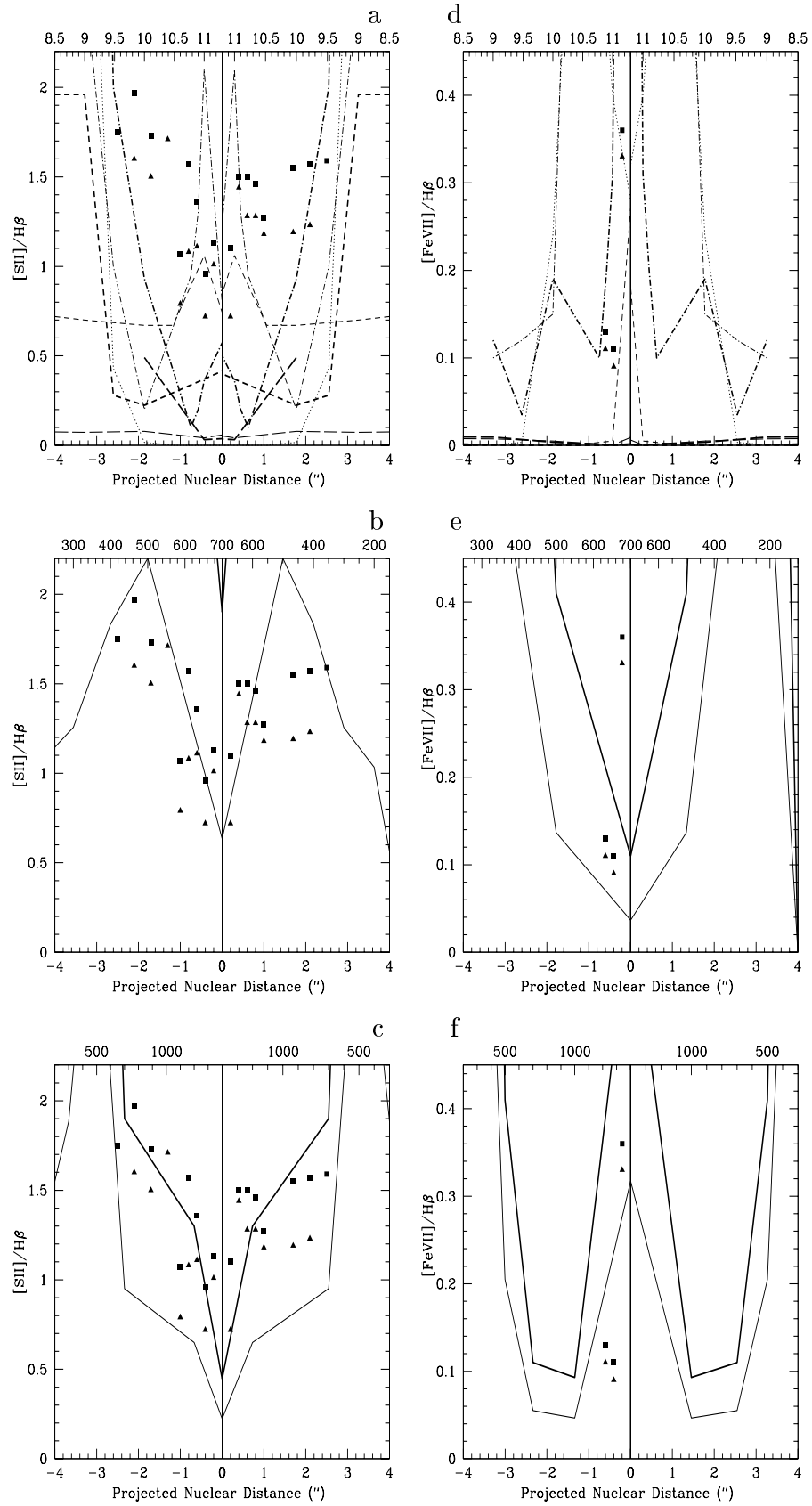


**Fig. 4.** The [S II] 6713+6731/H $\beta$  (left) and the [Fe VII] 6086/H $\beta$  (right) emission-line ratios as a function of the projected nuclear distance. Same notation as in Fig. 1.

a consistent picture over a large spatial distribution of several emission lines and the precision of the fit must be achieved.

#### Observed features

In several cases there are two or more emission lines within the passband, so that different velocities are sampled for the different lines (Hutchings et al. 1999). These are the [O II] 3727 and [S II] doublets, as well as [N II] lines plus  $H\alpha$  at about 6548 Å. The [O III] image covers velocities between  $-1200$  and  $-860$  km s $^{-1}$ . High velocity material in this velocity range is much fainter than the main bright clouds showing low velocities. It is seen on both sides of the nucleus and outside the main biconical emission regions. The high velocity gas is weak in  $H\beta$  and [O II] lines and seems to be associated with highly ionized material. Ionization of oxygen is higher along radial locations on both sides of the nucleus. Generally, there is an association of high velocity clouds with high ionization gas, however, there are regions of high ionization (mainly to the E side) with no known high velocity gas. Nelson et al. (2000) claim that the high velocity components generally account for a small fraction of the total flux in the [O III] emission lines. In several cases they find clouds with multiple velocity components.

#### 4.1. Oxygen lines: [O III], [O II], and [O I]

The results for [O III]/ $H\beta$  and [O II]/ $H\beta$  are shown in Fig. 2. Different models are selected to fit the data as expected from the multiple structure of the observed lines (Kaiser et al. 2000). As shown in Fig. 2a, the data are well reproduced by composite RD models, with the intensity of the ionizing radiation  $F_H$  decreasing by more than two orders of magnitude from the center towards the outskirts of the nuclear region.

Focusing on [O III]/ $H\beta$ , RD clouds (Fig. 2a) with velocities of 200–300 km s $^{-1}$  contribute preferentially in the inner 1 arcsec region, while those with velocities of 100 km s $^{-1}$  appear at larger distances from the center, in agreement with Winge et al. (1999). The contribution to [O III]/ $H\beta$  line ratios from RD clouds with  $V_s \sim 500$  km s $^{-1}$  is small.

Regarding the SD clouds (Figs. 2b and c), the high velocity ones ( $V_s > 500$  km s $^{-1}$ ) are responsible for only a few percent of the central region emission, while a larger contribution at 3'' from the center comes from the low velocity clouds ( $V_s < 500$  km s $^{-1}$ ).

The situation is markedly different regarding [O II]/ $H\beta$  (Figs. 2d, e, and f) as it appears dominated by SD models. The trend of [O II]/ $H\beta$  is nicely explained by SD models with  $V_s$  between  $\sim 400$  and 700 km s $^{-1}$  (thick line).

Recall that the contribution of high velocity clouds to the [O II]/ $H\beta$  line ratio is due to the diffuse radiation generated at the high temperature post-shock zone reaching the low ionization zone. In order to illustrate this, the distribution of the temperature as well as the

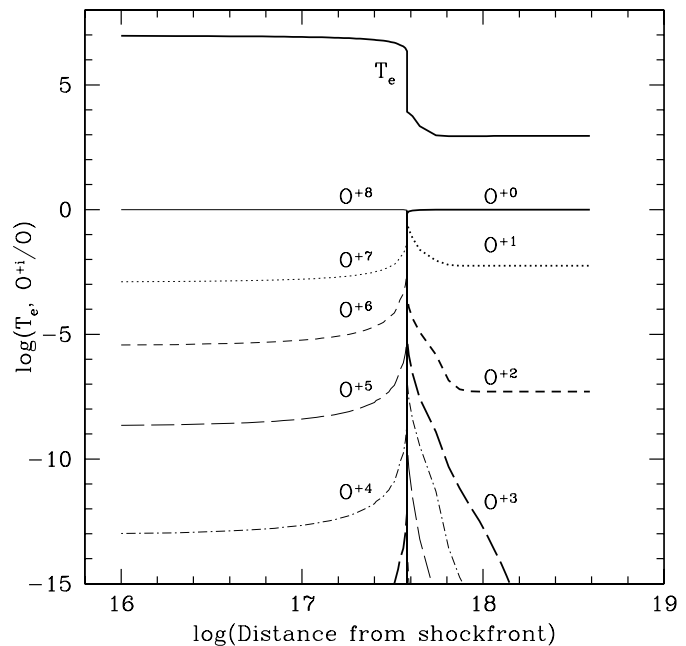


**Fig. 5.** The distribution of the electron temperature and of the ionic fractional abundance of oxygen downstream for a shock-dominated model ( $F_H = 0$ ) with  $V_s = 700$  km s $^{-1}$  and  $n_0 = 700$  cm $^{-3}$ . The shock front is on the left.

fractional abundance of oxygen ions downstream are plotted in Fig. 5 for an SD model with  $V_s = 700$  km s $^{-1}$ .

Notice, however, that explaining the [O II]/ $H\beta$  line ratio only with SD clouds may not be acceptable in a global picture for the NLR, since RD clouds must be present and contributing to other emission lines. Indeed, the reduction by a factor of 3 is not only dictated by the fit of the [O I]/ $H\beta$  data (Fig. 3b), but is consistent with a general scenario.

Regarding the [OI]/ $H\beta$  line ratio, notice that SD models overpredict the observed [O I]/ $H\beta$  data by a factor of  $\sim 3$ . This indicates that SD models with  $V_s \sim 700$  km s $^{-1}$  in the central region must be taken with a lower weight in an eventual averaged model. The shift of the SD models dictated by the [O I]/ $H\beta$  ratios is consistent with all the other lines.

#### 4.2. Sulphur lines: [S III] and [S II]

To further investigate NGC 4151 line emission we address a problem raised by Kraemer et al. (2000), namely, the overprediction of the [S III] 9069+9532 / $H\beta$  line ratio by photoionization models. This ratio is shown in Fig. 3.

Different clouds with different  $V_s$  coexist in the center. The larger values can be fitted by RD models with  $V_s \geq 500$  km s $^{-1}$ . Notice, however, that RD models with  $V_s = 500$  km s $^{-1}$  and  $\log F_H \leq 10.5$  overpredict the data in the region beyond 1'' at both sides of the center. Therefore, for consistency, they were taken out from all figures.

There is no contribution from SD clouds to the [S III]/ $H\beta$  ratio in the central region (Fig. 3e, f). On the other hand, a strong contribution to the [S II]/ $H\beta$  line

ratios comes from the SD clouds with rather high velocities ( $700 \text{ km s}^{-1}$ ) in the central region, and a not negligible contribution of SD clouds with  $V_s = 1000 \text{ km s}^{-1}$  (Fig. 4c), as for the case of  $[\text{O II}]/\text{H}\beta$ . Here too the signature of the diffuse radiation generated at the high temperature post-shock zone is seen.

From the  $[\text{S II}]6717/6731$  diagrams of Nelson et al. (2000, Fig. 10), the gas is rather clumpy and also indicates a decrease in density with distance. The data in the outer region ( $>2''$ ) are well explained by RD models with  $V_s = 100 \text{ km s}^{-1}$  and  $n_0 = 100 \text{ cm}^{-3}$ , leading to  $[\text{S II}] 6716/[\text{S II}] 6730 \geq 1$ . Density downstream decreases for lower shock velocities and lower preshock densities (see Contini & Aldrovandi 1986), therefore,  $[\text{S II}] 6716/[\text{S II}] 6730 \geq 1$  is expected in the regions farther from the center. In fact, we have found that velocities generally decrease with distance from the center. However, some ratios of about 0.5 are given by Nelson et al. They are supported by the fact that some models with  $V_s$  of about  $500 \text{ km s}^{-1}$  also fit the data beyond  $1''$  (Figs. 4b and c).

#### 4.3. The $[\text{Fe VII}]$ line

Fe coronal lines are usually underpredicted by pure photoionization models. In the case of NGC 4151,  $[\text{Fe VII}]/\text{H}\beta$  is underpredicted by a factor of  $\sim 3$  by Kraemer et al. (2000) and by Alexander et al. (1999). To explain the discrepancy, an overabundance of Fe is often suggested, which is somewhat surprising since a fraction of Fe may be locked in grains, although sputtering is strong for small grains and high velocity shocks.

$[\text{Fe VII}]/\text{H}\beta$  values for  $\text{PA} = 221^\circ$  are shown in Figs. 4d, e, and f. The available data are scarce, hence further constraints to the models are really not possible. The models used to fit the other lines are compared with the available data. As seen in Fig. 4f high velocity models overpredict the  $[\text{Fe VII}]/\text{H}\beta$  line ratio. A better fit is obtained reducing the weight of the high velocity models by a factor of 2. This reduction does not change our discussion above concerning the other lines, because models with  $V_s = 1400 \text{ km s}^{-1}$  contribute by no more than 20% to  $[\text{O II}]/\text{H}\beta$  and  $[\text{S II}]/\text{H}\beta$  line ratios. As we will see over the next sections, a low contribution from high velocity clouds is also needed to explain the IR lines (Sect. 6) and the continuum SED (Sect. 7). Notice that the  $[\text{Ne V}] 3426$  lines, also coming from the high ionization zone in the clouds, are overestimated by high velocity models (see Sect. 5).

#### 5. The Ne and Si infrared lines

The ISO coronal line data reported by Sturm et al. (1999) are used to further constrain the models. Since the ISO aperture are of the order of several arcminutes, only the coronal lines are used. Lines from lower ionization stages may include the contribution from star forming regions in the galaxy. Nevertheless, they are included in the discussion in order to complete the data set with information from different ionization stages.

Two Ne coronal lines are observed:  $[\text{Ne VI}] 7.6$  and  $[\text{Ne V}] 14.3$  in addition to two other strong lines,  $[\text{Ne III}] 15.5$ , and  $[\text{Ne II}] 12.8$ . Regarding Si,  $[\text{Si IX}] 3.94$ ,  $[\text{Si VII}] 2.48$ , and  $[\text{Si II}] 34.8$  are detected.

From all the models plotted in Figs. 2 to 4, we select those which could better reproduce the IR line ratios. The corresponding input parameters are listed in Table 1, as well as the weights ( $W(\text{Ne})$ ) adopted for the best average model (AV). The weights are relative to that of model 2.

The weights adopted for the Si lines ( $W(\text{Si})$ ) are, however, different because they account for Si depletion from the gas phase (and included in grains), which is different in each model. To account for the Si coronal line emission, Si/H has to be depleted by a factor of about 15. Moreover, the different depletion of Si in the different clouds may be indicating that the dust is not homogeneously distributed in the emitting clouds (see Kraemer et al. 2000).

Notice that the weights are very different for different models because they must compensate the difference by many orders of magnitude of the line intensity fluxes, in order to obtain similar contribution to the emission lines from different models (CV01). SD and RD clouds correspond respectively to models 2, 3, 4, 6, and models 1 and 5.

The observed IR emission-line flux as well as the ratios of the calculated to observed lines are listed in Table 2. This table is organized as follows: (a) line fluxes (row 1); (b) the results corresponding to the best fit model of Alexander et al. (1999) (row 2); (c) single-cloud results (rows 3 to 8); (d) the weighted average model AV (row 9); (e) the contribution to the IR emission lines from each single-cloud model (rows 10 to 15).

Actually, the line and continuum spectra must be modeled consistently, so, the results of the AV model in Table 2 are cross-checked by the results of the continuum SED in Sect. 7, until the best tuning for both is achieved.

Because the theoretical fluxes are calculated at the nebula and the observed fluxes are measured at Earth, the ratio of the square distance of the galaxy to Earth ( $d^2$ ) to the square distance of the nebula to the galaxy center ( $R^2$ ) is given in the last column of Table 2.

From Table 2, one sees that model 2 (SD,  $V_s = 300 \text{ km s}^{-1}$ ) strongly contributes to all the lines. Gas is heated to temperatures between  $1.3 \times 10^6 \text{ K}$  and  $3.7 \times 10^6 \text{ K}$  for SD clouds with  $V_s$  of  $300 \text{ km s}^{-1}$  and  $500 \text{ km s}^{-1}$ , respectively. Radiation dominated model 1 contributes mainly to  $[\text{Ne V}]$  and  $[\text{Si II}]$  and model 5 to  $[\text{Ne III}]$  and  $[\text{Si VII}]$ . Model 5 is associated with a very high ionizing flux:  $5 \times 10^{12} \text{ cm}^{-2} \text{ s}^{-1} \text{ eV}^{-1}$  at the Lyman limit).

The high velocity clouds (model 6,  $V_s = 1500 \text{ km s}^{-1}$ ) do have a low contribution. This contribution must remain low as to prevent the increase of  $[\text{Si IX}]$  flux far beyond its observational value.

#### 6. The UV line ratios

Ultraviolet lines may provide important information about their origin in a gas either heated by shocks or

**Table 1.** The models for the infrared lines.

model	1	2	3	4	5	6
$V_s(\text{km s}^{-1})$	100	300	500	500	500	1500
$n_0(\text{cm}^{-3})$	100	300	300	300	300	300
$\log F_H$	11	-	-	-	12.7	-
$D(10^{17} \text{ cm})$	100	100	10	100	100	1
$W(\text{Ne})$	5.(-4)	1.	6.5(-4)	7.9(-4)	2.(-6)	2.9(-8)
$W(\text{Si})$	0.114	1.	1.4(-3)	1.43(-3)	1.4(-4)	1.6(-6)

**Table 2.** The infrared lines relative to the observation data.

	[Ne VI]	[Ne V]	[Ne III]	[Ne II]	[Si IX]	[Si VII]	[Si II]	$d^2/R^2$
fluxes (obs) <sup>1</sup>	7.90	5.50	20.7	11.8	0.41	1.2	15.6	-
model (calc/obs) <sup>2</sup>	0.5	1.8	0.7	0.5	0.9	0.4	3.	-
model 1 (calc <sup>3</sup> /obs)	2.30	10.3	2.39	0.017	0.064	0.137	80.4	10 <sup>11</sup>
model 2 (calc/obs)	1.20	0.40	0.50	0.90	17.6	3.90	6.6	10 <sup>9</sup>
model 3 (calc/obs)	1.80	0.70	6.80	11.2	205.	11.1	36.7	10 <sup>9</sup>
model 4 (calc/obs)	1.80	0.70	6.70	11.0	199.	10.6	27.7	10 <sup>9</sup>
model 5 (calc/obs)	1.98	15.0	27.5	0.92	3.70	5.42	0.11	10 <sup>13</sup>
model 6 (calc/obs)	2.05	1.53	0.16	0.01	1.04e5.	240.	0.0	10 <sup>9</sup>
model AV (calc <sup>4</sup> /obs)	1.30	1.24	1.19	0.92	1.44	0.80	1.0	-
model 1%	8.70	42.8	10.3	0.09	3.04	11.9	57.3	-
model 2%	88.3	32.3	42.0	97.7	72.7	29.4	41.2	-
model 3%	0.01	0.0	0.04	0.08	1.21	0.12	0.33	-
model 4%	0.01	0.0	0.04	0.09	1.18	0.11	0.25	-
model 5%	3.00	24.9	47.5	2.05	21.8	58.5	0.98	-
model 6%	0.0	0.0	0.00	0.0	0.06	0.0	0.0	-

<sup>1</sup> In  $10^{-13} \text{ erg cm}^{-2} \text{ s}^{-1}$ <sup>2</sup> Alexander et al.<sup>3</sup> Calculated at the nebula<sup>4</sup> To calculate the averaged model from the models given in CV01:  $\sum_i [(F(\lambda)/F(\text{H}\beta))_{\text{CV01}} F(\text{H}\beta)_{\text{CV01}}] W(\text{model } i)] / F(\lambda)_{\text{obs}}$ 

ionized by a strong radiation. The most significant lines are N V 1240, C IV 1550, and He II 1640. Other strong UV lines are generally blended (O IV, Si IV 1402, C III], Si III] 1909, etc.), and have not been used in the modeling. Because the reddening correction in the UV is important, we use the N V/C IV and He II/C IV line ratios instead of intensities relative to H $\beta$ .

The UV data correspond to PA = 221° observations. Model results are presented in Fig. 6 where South-West (SW) data (filled triangles) are separated from those from the North-East (NE) region (open triangles).

The theoretical results indicate that the NE UV data can be explained by low velocity RD clouds ( $<300 \text{ km s}^{-1}$ ) reached by an ionizing flux  $F_H < 10^{11}$  units, while the SW UV data come from the RD clouds reached by a stronger radiation field, with some contribution from SD clouds with  $V_s > 500 \text{ km s}^{-1}$ . However, these results are only indicative (see the discussion by Kraemer et al. 2000). It is well known that the He II 1640 line is strongly dependent on the spectral index of the ionizing radiation, and the N V/C IV ratio depends on the adopted N/C abundance ratio. Regarding the He II lines, if  $\alpha_{\text{UV}} < 1.5$  the theoretical results may vertically shift to the upper part of the diagram, and the derived velocities would be larger.

Regarding the N/C abundance ratio, the cosmic values is adopted.

For consistency, we present in Table 3 the observed/calculated UV-optical line ratios obtained with the same AV model as for the IR lines (see Table 2). To avoid the uncertainty of the dilution factor the ratios of the AV model are calculated between the line ratios to H $\beta$ .

The fit is within 1.6 and the trend is always to overestimate the values. This is consistent with reduction of the SD models which was adopted in Figs. 2–4b, c, and e, f.

## 7. The continuum

To further constrain our model for NGC 4151, the continuum SED is analysed and modeled using the composite model derived from the Ne and Si lines in Sect. 5.

### 7.1. Observations

Gamma-rays to the optical continuum emission is taken from the 1993 December multiwavelength monitoring campaign of NGC 4151 (Edelson et al. 1996). The source was near its peak historical brightness during this campaign and showed the strongest variations of its

**Table 3.** The UV-optical lines

	[Ne IV]2423	[Ne V]3426+	[Ne III]3869+	He II 4686	[O III]4363	[N II]6584+
fluxes (obs) <sup>1</sup>	1.77	1.56	1.81	0.31	0.35	2.16
model (calc/obs) <sup>2</sup>	0.4	1.5	0.8	1.1	0.7	0.8
model (calc/obs) <sup>3</sup>	-	-	0.5	1.1	-	1.8
model AV (calc/obs)	1.3	1.5	1.5	1.1	1.6	1.4

<sup>1</sup> In  $10^{-15}$  erg  $\text{cm}^{-2}$   $\text{s}^{-1}$  (Kraemer et al 2000, Table 1, 0'1–0'3).

<sup>2</sup> Kraemer et al. (2000, Table 1, 0'1–0'3).

<sup>3</sup> Alexander et al. (1999).

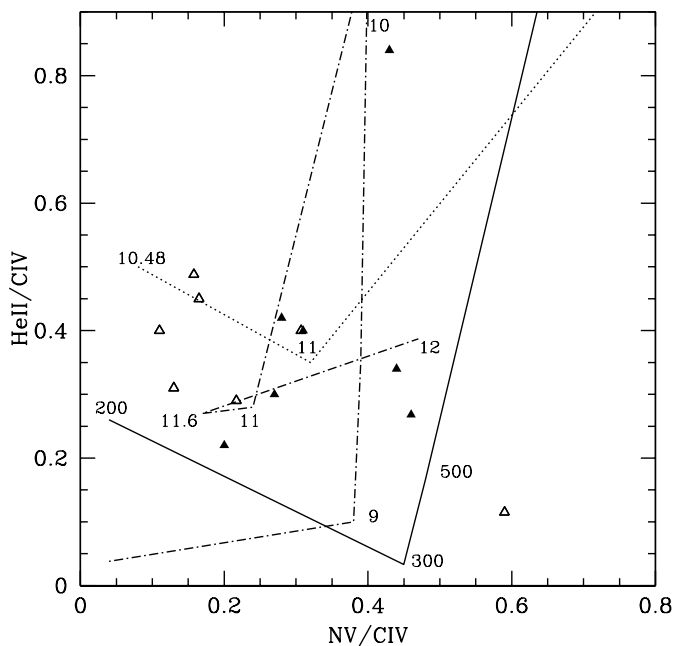


**Fig. 6.** He II 1640/C IV 1550 versus N V 1240/C IV 1550. SW UV data and NE UV data correspond, respectively, filled and empty triangles. The RD results for  $V_s = 100$   $\text{km s}^{-1}$  and  $n_0 = 100$   $\text{cm}^{-3}$  (dotted line), and  $V_s = 200$   $\text{km s}^{-1}$  and  $n_0 = 200$   $\text{cm}^{-3}$  (dash-dotted line) are labelled by the values of  $\log(F_H)$ , and the SD results (solid line) by  $V_s$  in  $\text{km s}^{-1}$ .

continuum emission at medium energy X-rays ( $\sim 1.5$  keV) with amplitude variations of 24%, weaker variations (6%) at the gamma-ray energies, decreasing variation from ultraviolet (9%) to optical (1%) and finally, not significant variation at the soft X-rays (0.1–1 keV).

Assuming that the continuum emission variations are within a few percent level beyond optical wavelengths, the 1993 data are combined with IR data taken at different epochs. Since the optical aperture used by Edelson et al. (1996) is  $12 \times 3$  arcsec, near-IR fluxes from an aperture size of 10 arcsec is adopted when possible. Sources are as follows:

The data for the near-IR come from the NASA Extragalactic Data (NED),  $J$ ,  $H$  and  $K$  data are taken from Balzano & Weedman (1981) and  $L$  and  $M$  data from McAlary et al (1979). The 10 microns emission is from Lebofsky & Rieke (1979) and corresponds to an aperture

size of 6 arcsecs. In addition, to trace the non-stellar contribution at the near-IR, Kotilainen's et al. (1992) data within a 3 arcsec aperture are also considered for comparative purposes.

For the far-IR region between 16 and 200 microns, ISOPHOT data from Perez-Garcia et al. (1998) are taken. Due to the large aperture size used in ISOPHOT, those data are integrated over the complete galaxy.

For the radio data, values at 1.4 GHz, 4.85 GHz, and 408 MHz were at the NED, and come from Becker et al. (1995), Becker et al. (1991), and Ficarra et al. (1985), respectively, while data at 8.4 and 5 GHz are taken from Pedlar et al. (1993).

Compared with other Seyfert galaxies, NGC 4151 is relatively weak in X-rays with  $L(2-10 \text{ keV}) \sim 7 \times 10^{42}$  erg  $\text{s}^{-1}$  (Weaver et al. 1994). The soft X-ray emission is extended (Morse et al. 1995). Recent Chandra data resolve up to  $\sim 70\%$  of the 0.4–2.5 keV emission (Ogle et al. 2000). This emission appears to be associated with the optical narrow line gas (NLR) extending asymmetrically to the South-West of the nucleus.

## 7.2. On the nature of the soft X-ray emission

Both, Weaver et al. (1994) and Ogle et al. (2000) provide similar estimates for the plasma pressure of the hot gas of about  $3 \times 10^7$   $\text{cm}^{-3}$  K. This is one order of magnitude larger than the pressure derived from the cold NLR gas (Penston et al. 1990). The difference strongly argues against the soft X-ray emission being associated with the NLR confining medium (Weaver et al. 1994; Ogle et al. 2000).

Weaver et al. (1994) also found that the Fe K edge energy in their 0.4–11 keV data (from the BBXRT mission) is inconsistent with an origin in a gas with the same ionization parameter as the low-energy absorber. This allows the authors to rule out a line-of-sight ionized absorber as the sole source of the soft X-ray excess in NGC 4151 (see also Contini & Viegas 1999 for the case of NGC 4051).

George et al. (1998) propose a model for the 0.2–10 keV spectrum where the underlying power law nuclear component is partially absorbed by an ionized absorber and partially scattered. However, it requires an additional component due to Bremsstrahlung thermal emission from an extended photoionized gas at  $T \sim 6 \times 10^6$  K.

Recent Chandra data provide direct evidence of X-ray line emission gas at  $T \sim 10^7$  K. The strength and ionization potential of the X-ray narrow emission lines indicate a composite spectrum in which both photoionization and shocks are at work (Ogle et al. 2000). The fair spatial association between the central NLR optical region and the soft X-ray emission indicated that both mechanisms are contributing to the multi-wavelength SED and to the line spectrum of NGC 4151 (cf. Komossa 2001). Taking into account these observational constraints, the origin of this soft X-ray excess is evaluated in the next section assuming high velocity models dominated by shocks.

### 7.3. Model results

NGC 4151 shows the characteristics of Seyfert galaxies rather than starbursts. Therefore, we consider that the continuum SED is Bremsstrahlung radiation from clouds ionized and heated by the radiation from the AC and by shocks. We refer to previous studies (e.g. Contini & Viegas-Aldrovandi 1990; Contini & Viegas 1991; Viegas & Contini 1994; Contini & Viegas 2000, etc.) on this subject which could lead to a better understanding of the results. Particularly, dust and gas are coupled entering the shock front and mutually heat each other. The grains are collisionally heated to the highest temperatures ( $\geq 300$  K) leading to emission in the near-IR. On the other hand, heating by the central radiation is not efficient enough, so dust in the radiation dominated zone does not reach such high temperatures.

Before discussing model results, let us notice that below the Lyman limit, up to say 0.2 keV, we have very little observational information: this is the “unknown window” where observations are difficult because of the heavy absorption by our Galaxy. However, in the 0.2 to 2 keV region, NGC 4151 shows extended emission, spatially correlated with the optical NLR gas. If due to Bremsstrahlung, the tail of this X-ray emission should somehow show up in the far UV. However, no detected extended emission appears in the UV HST images of NGC 4151 (Boksenberg et al. 1995). Therefore, the emission from the NLR gas should be lower than that of the UV nucleus of NGC 4151. We will use this observational fact as a constraint in the proposed modeling in the sense that the observed nuclear UV emission can only be associated with model emission within a nuclear region of outmost 3 pc size.

Observational data and model results are plotted in Figs. 7 and 8, which refer to models and relative weights adopted to fit the Ne infrared lines (Table 1, row 5). Notice that Bremsstrahlung peaks at high frequencies depending on  $V_s$  (see Viegas & Contini 1994).

The large geometrical thickness of the emitting clouds and the high densities downstream due to compression ( $n/n_0 \geq 10$ , depending on  $V_s$ ,  $n_0$ , and  $B_0$ ) lead to high optical thickness of the emitting gas with column densities of the order of  $10^{21}$ – $10^{24}$   $\text{cm}^{-2}$ . This is within the range of column densities estimated from the X-ray

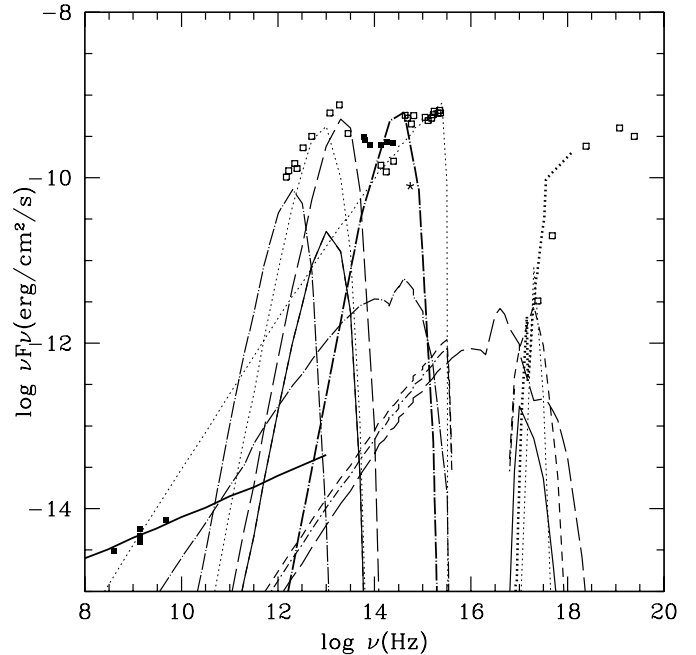


**Fig. 7.** Different components contributing to the SED of the continuum of NGC 4151, corresponding to the results of several models, scaled following the weights used to fit the IR lines. The models are the following: 1 (dash-dotted line), 2 (dotted line), 3 (short dash-dotted line), 4 (short-dashed line), 5 (solid line), 6 (long dashed line). The flux from the AC in the far X-rays, which is seen through the clouds, is represented by a thick dotted line, while the continuum from the old stellar population is indicated by a thick long dash-dotted line. The theoretical results are compared to observational data taken from the NED (filled squares) and from other sources described in Sect. 7 (open squares).

data,  $\sim 5 \times 10^{22}$   $\text{cm}^{-2}$  (Weaver et al. 1994; George et al. 1998; Ogle et al. 2000). Accordingly, the emitted radiation gets absorbed in the cloud itself between  $\sim 13.6$  eV and 500 eV, hence the emission gap in this region shows up in Figs. 7 and 8. The high velocity model 6 has however a lower column density ( $< 10^{21}$   $\text{cm}^{-2}$ ) because is radiation-bounded. In fact, due to strong compression, the temperature rapidly decreases downstream at a distance  $< 10^{16}$  cm from the shock front. Thus, the contribution of model 6 to the SED extends into the far UV range (Fig. 7 long-dashed line). However, the X-ray data in the frequency range  $10^{15}$  and  $10^{17}$  Hz impose a limit on the relative contribution of this model 6 (see below). All together, the fit of the continuum at the UV range is obtained with model 2. The dust-to-gas ratio that characterizes this model is  $d/g = 10^{-14}$ . The other models (models 3, 4, 5, and 6) underpredict the data.

The summed SED which better explains the observations is shown in Fig. 8. The main components are summed separately: radio emission, reradiation by dust in the IR, gas Bremsstrahlung, and the flux from the active source. Moreover, as was found for many Seyfert galaxies (see Contini & Viegas 2000) a black-body with temperature of  $\sim 3000$  K is used to roughly represent the

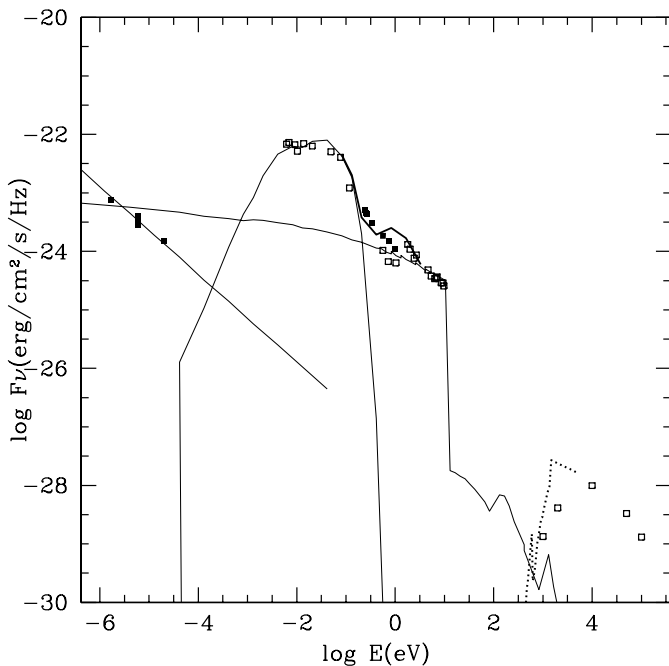


**Fig. 8.** The continuum spectrum of NGC 4151. The thin solid lines correspond to the summed theoretical contributions from dust emission, gas Bremsstrahlung and radio emission as shown in Fig. 7. The thick solid line corresponds to the summed contributions from dust emission, gas Bremsstrahlung and the old stellar population continuum, while the dotted line corresponds to the AC continuum seen through the clouds. The observational data are taken from the NED (filled squares) and from other sources described in Sect. 7 (open squares).

optical continuum due to the stellar population (thick solid line).

Notice that we are interested in the bulk contribution of the stars rather than the detailed shape of their continuum emission. Thus, although we could use the spectrum of an early-type galaxy or the spectrum of the central region of a Sa galaxy to get a more realistic fit of the stellar contribution, it would not change our conclusions.

For instance, Malkan & Filippenko (1983) find that about 1/10 of the emission at 5500 Å and  $\sim 1/3$  at 9000 Å are due to stars (in aperture of  $10''$ , just the same aperture of the optical and IR data used in this paper), namely they estimated the stellar emission to be 14 mJy at 5500 Å. We have added the corresponding value to Fig. 7 (star). Accounting for the errors in the observations and models, notice the good agreement (within 30%) with the black body emission curve.

The bump in the IR is rather wide, representing the sum of contributions from different models. In previous papers (e.g. Contini et al. 1999b, Appendix A) it was explained that the bump in the IR due to each model depends on the shock velocity. Particularly, the high velocity model (model 6) has its maximum at the near-IR. To fit the near-IR data, a high  $d/g$  ( $2 \times 10^{-12}$ ) is assumed in model 6, indicating that high velocity material is rather dusty. A shock velocity of  $1500 \text{ km s}^{-1}$  produces a post

shock region at a temperature of  $3.4 \times 10^7 \text{ K}$ , in agreement with the hot plasma temperatures derived from the X-ray data, indicating that high velocity material is rather dusty.

Shocked clouds with  $V_s \sim 700 \text{ km s}^{-1}$  produce lower temperatures,  $\sim 10^6 \text{ K}$ , which are still within the range of values estimated from X-ray data (e.g. George et al. 1998). These velocities are also revealed by optical lines (Sect. 4).

Yet, the contribution of a model with  $V_s = 1500 \text{ km s}^{-1}$  in the SED should be taken with a relative small weight ( $\leq 2.9 \times 10^{-8}$ ), because the data in the soft X-ray range constrain the model. As a consequence, the contribution of this model to the IR lines is very low. Thus, a signature of these high velocity clouds is not expected to be seen in the infrared emission-line spectrum.

In the radio range, Pedlar et al. (1993) derive an average spectral index for the entire source of  $\alpha = -0.87$  from their 8.4 and 5 GHz data. They interpreted the emission as due to thermal free-free emission from the NLR. In the present modeling, the radio data are instead well explained by synchrotron radiation with spectral index  $-0.75$ , generated by Fermi mechanism at the shock front (Bell 1978). Notice that self-absorption of the Bremsstrahlung emission at these radio wavelengths may be important, hence its contribution is negligible (see, for instance Contini et al. 1998b).

## 8. Discussion and conclusions

In this paper we have modeled the narrow emission-line and continuum spectra of NGC 4151 with particular attention to the large range of velocities indicated by the line profiles.

The analysis of the line profiles is complex and clouds in many different conditions can contribute to each line. By modeling the NLR to analyse the high spatial resolution data (Nelson et al. 2000; Kraemer et al. 2000), it is found that the contribution of each cloud to a given line may show a large variation from line to line.

In the central region high velocity clouds revealed by the observations (Hutchings et al. 1999; Winge et al. 1997, etc.) are shock dominated (SD). There is a strong contribution of SD clouds with shock velocity  $V_s \sim 700 \text{ km s}^{-1}$  to [O II] 3727/H $\beta$ , and [O I] 6300/H $\beta$ . Radiation dominated (RD) clouds with  $V_s \sim 500 \text{ km s}^{-1}$  are necessary to explain [S III]/H $\beta$  and [O I]/H $\beta$ , while clouds with low  $V_s$  ( $100\text{--}200 \text{ km s}^{-1}$ ) and reached by a relatively strong ionizing radiation ( $\log F_H \sim 11$ ) contribute to the [O III]/H $\beta$ , [O II]/H $\beta$ , and [S II]/H $\beta$  line ratios.

Beyond  $2''$  from the center, RD clouds, photoionized by a weaker radiation flux are responsible for the observed line emission.

Quantitative modeling of the Ne and Si infrared lines from different ionization levels leads to more results. Notice, however, that the observations give the integrated flux from all the galaxy, so that it is not possible to understand which type of clouds prevail in different regions.

SD clouds with  $V_s = 300 \text{ km s}^{-1}$  strongly contribute to all Ne lines corresponding to different ionization levels (Table 2), while RD clouds with velocities of  $500 \text{ km s}^{-1}$  and reached by a strong radiation flux ( $\log F_H = 12.7$ ) contribute particularly to the [Ne III] and [Si VII] IR lines. Due to the high postshock temperature, high velocity clouds ( $V_s = 1500 \text{ km s}^{-1}$ ) would overpredict the [Si IX] 3.94 line. Therefore, the contribution of these clouds is low. A large contribution to [Ne V] and [Si II] lines come from low velocity ( $100 \text{ km s}^{-1}$ ) clouds reached by an ionizing radiation characterized by  $\log F_H = 11$ .

Modeling of the IR lines also shows that silicon is depleted by a factor of 15 because included in dust grains, while N/C abundance ratio is found compatible with cosmic values from the modeling of the UV lines.

Comparing the results of the present work with those of other authors, notice that our results are slightly better. Indeed, better fits could be obtained with a different choice of weights. However, the results presented in Tables 2 and 3 are consistent with the fit of the continuum SED (Sect. 7) and were chosen accordingly. More particularly, it seems that the three Ne emission lines are higher than observed by factors of 1.3–1.5. This may be an indication that the Ne abundance we have used is a factor of 1.3–1.5 too high. So, decreasing the Ne/H abundance by 1.3, we get a better agreement. The He II 4686 line is slightly higher, but this is mainly due to the power law above 54.4 eV, which we (and the others) could have taken somehow too flat. The only problem is the [O III] 4363 line. Because oxygen is a coolant, changing the O abundance may not solve the problem. However, a factor of 1.6 higher is still within the limit of a factor of 2 proposed by Alexander et al., who do not give their results for [O III] 4363.

Notice that we based our models on IR lines and we compared with Alexander et al. (1999). So, we should refer only to them. The results of Kraemer et al in row 2 of Table 3 are better than ours only for [O III] 4363 and [Ne III]. Actually, they come from observations in the region between  $0.1''$  and  $0.3''$  SW, whereas we average on all the regions.

The analysis of the continuum SED leads to the following results:

The high velocity material is very dusty ( $d/g \sim 10^{-12}$ ). The radio emission is synchrotron created by Fermi mechanism at the shock front. Moreover, shocks are important to explain the soft X-rays: shocks with velocities of  $1500 \text{ km s}^{-1}$  produce a post shock region at a temperature of  $3.4 \times 10^7 \text{ K}$ . This value is in agreement with the temperature found by Weaver et al. (1994) and Ogle et al. (2000) for a non-equilibrium plasma from X-ray observations, while clouds with  $V_s \sim 750 \text{ km s}^{-1}$  produce temperatures of  $8 \times 10^6 \text{ K}$  (George et al. 1998).

An estimate of several physical quantities applying to the central AGN region can be derived from the proposed modeling.

If  $d$  is the distance from Earth (19.8 Mpc) and  $d^2/R^2 = 10^9$  (see Table 2),  $R \sim 0.626 \text{ kpc}$  is the average distance of

the emitting nebula to the AC. Adopting an average downstream density  $n = 10^5 \text{ cm}^{-3}$ , and  $D = 10^{18} - 10^{19} \text{ cm}$ , the calculated mass is  $M \sim 3.5 \times 10^{8-9} \text{ ff } M_\odot$ , where ff is the filling factor which is likely to be less than unity. In this case our estimation of the NLR mass is lower than the values quoted by Ulrich (2000) for an emitting region closer to the center, i.e.  $10^9 M_\odot$  within 40 pc and  $5 \times 10^7 M_\odot$  within 12 pc ( $0.15''$ ). The corresponding calculated central source luminosity is about  $1.6 \times 10^{43} \text{ erg s}^{-1}$ . The average kinetic energy of the NLR is about  $3 \times 10^{56} \text{ ff ergs}$ , assuming an average velocity of the NLR clouds of  $300 \text{ km s}^{-1}$ . This would imply that the time scale for the AGN phase in NGC 4151 should be larger than  $5 \times 10^5$  years.

Summarizing, we provide a self-consistent modeling of the multiwavelength line spectrum and SED of the nuclear region of NGC 4151.

The modeling is based on the coupled effect of shocks and photoionization operating in the narrow emission line gas. As such, it implies the existence of emitting clouds with velocities and densities in a large range. An emitting-cloud distribution in the velocity/density space is precisely what is revealed by the HST observations of this galaxy. This together with the fair fitting of the line and continuum spectra obtained in this work reinforces our hypothesis that shocks and photoionization are effectively coupled in the NLR of AGN.

*Acknowledgements.* We are grateful to the referee for many helpful comments. This paper is partially supported by the Brazilian agencies: CNPq (304077/77-1), PRONEX/Finep (41.96.0908.00), and FAPESP (00/06695-0).

## References

- Alexander, T., Sturm, E., Lutz, D., Sternberg, A., Netzer, H., & Genzel, R. 1999, ApJ, 512, 204
- Balzano, V. A., & Weedman, D. W. 1981, ApJ, 243, 756
- Becker, R., White, R., & Helfand, D. 1995, ApJ, 450, 559
- Becker, R., White, R., & Edwards, A. 1991, ApJS, 75, 1
- Bell, A. R. 1978, MNRAS, 182, 443
- Boksenberg, A., Catchpole, R. M., Macchetto, F., et al. 1995, ApJ, 440, 151
- Contini, M., & Aldrovandi, S. M. V. 1986, A&A, 168, 41
- Contini, M., & Viegas-Aldrovandi, S. M. 1990, ApJ, 350, 125
- Contini, M., & Viegas, S. M. 1991, ApJ, 373, 405
- Contini, M., & Viegas, S. M. 1999, ApJ, 523, 114
- Contini, M., & Viegas, S. M. 2000, ApJ, 535, 721
- Contini, M., & Viegas, S. M. 2001, ApJS, 132, 211 (CV01)
- Contini, M., Prieto, M. A., & Viegas, S. M. 1999a, ApJ, 492, 511
- Contini, M., Prieto, M. A., & Viegas, S. M. 1999b, ApJ, 505, 621
- Crenshaw, D. M., Kraemer, S. B., Hutchings, J. B., et al. 2000, AJ, 120, 1731
- Ficarra, A., GruEFF, G., & Tommasetti, G. 1985, A&AS, 59, 255
- George, I. M., Turner, T. J., Netzer, H., et al. 1998, ApJS, 114, 73
- Hutchings, J. B., Crenshaw, D. M., Kaiser, M. E., et al. 1998, ApJ, 492, L115

- Hutchings, J. B., Crenshaw, D. M., Dank, A. C., et al. 1999, *AJ*, 118, 210
- Kaiser, M. E., Bradley, L. D., II, Hutchings, J. B., et al. 2000, *ApJ*, 528, 260
- Komossa, S. 2001, *A&A*, 371, 507
- Kotilainen, J. K., Ward, M., Boisson, C., Depoy, D. L., & Smith, M. G. 1992, *MNRAS*, 256, 149
- Kraemer, S. B., Crenshaw, D. M., Hutchings, J. B., et al. 2000, *ApJ*, 531, 278
- Lebofsky, M. J., & Rieke, G. H. 1979, *ApJ*, 229, 111
- Malkan, M. A., & Filippenko, A. V. 1983, *ApJ*, 275, 477
- McAlary, C. W., McLaren, R. A., & Crabtree, D. R. 1979, *ApJ*, 234, 471
- Morse, J., Wilson, A., Martin, E., & Weaver, K. 1995, *ApJ*, 439, 121
- Nelson, C. H., Weistrop, D., Hutchings, J. B., et al. 2000, *ApJ*, 531, 257
- Ogle, P., Marshall, H. L., Lee, J. C., & Canizares, C. 2000, *ApJ*, 545, L810
- Osterbrock, D., & Koski, A. 1976, *MNRAS*, 176, P61
- Pedlar, A., Kukula, M. J., Longley, D. P. T., et al. 1993, *MNRAS*, 263, 471
- Penston, M. V., & Pérez, E. 1984, *MNRAS*, 211, 33p
- Perez-Garcia, A. M., Rodriguez Espinoza, J. M., & Santolaya Rey, A. E. 1998, *ApJ*, 500, 685
- Rieke, G. H., & Low, F. J. 1972, *ApJ*, 176, L95
- Schulz, H. R. 1988, *A&A*, 203, 233
- Schulz, H. R. 1990, *AJ*, 99, 1442
- Sturm, E., Alexander, T., Lutz, D., et al. 1999, *ApJ*, 512, 197
- Ulrich, M. H. 2000, *A&AR*, 10, 135
- Viegas, S. M., & Contini, M. 1994, *ApJ*, 428, 113
- Weaver, K. A., Mushotzky, R. F., Arnaud, K. A., et al. 1994, *ApJ*, 423, 621
- Weyman, R. J., Morris, S. L., Gray, M. E., & Hutchings, J. B. 1997, 483, 717
- Winge, C., Axon, D. J., Macchetto, F. D., & Capetti, A. 1997, *ApJ*, 487,
- Winge, C., Axon, D. J., Macchetto, F. D., Capetti, A., & Marconi, A. 1999, *ApJ*, 519, 324